

Optical Spectroscopy of Dwarf Galaxies at $z \sim 0.15$ in the COSMOS Field: Star Formation and Dust Properties

ZAHRA SATTARI,^{1,2,3} DANIEL D. KELSON,² BAHRAM MOBASHER,³ NIMA CHARTAB,¹ VIHANG MEHTA,¹ HARRY I. TEPLITZ,¹
AND SHANNON G. PATEL²

¹*IPAC, California Institute of Technology, 1200 E. California Blvd, Pasadena, CA 91125, USA*

²*The Observatories of the Carnegie Institution for Science, 813 Santa Barbara St., Pasadena, CA 91101, USA*

³*Department of Physics and Astronomy, University of California, Riverside, 900 University Ave, Riverside, CA 92521, USA*

ABSTRACT

We present a spectroscopic study of low-mass galaxies (LMGs; $10^8 \leq M_*/M_\odot \leq 10^9$) at $z \sim 0.15$ in COSMOS field, and compare it to a control sample of intermediate-mass galaxies (IMGs; $10^9 \leq M_*/M_\odot \leq 10^{10}$) at $z \sim 0.35$. We examine their star formation rates (SFRs), dust attenuation properties, and the relationship between nebular and stellar reddening. For both samples, SFRs derived from H α are strongly correlated with SFRs from fitting simple star formation histories (SFHs) to the galaxies' spectral energy distributions. In fitting a joint SFR– M_* relation, we obtain a slope of $\Delta\log(\text{SFR}_{\text{H}\alpha})/\Delta\log(M_*/M_\odot) = 1.01 \pm 0.03$, indicating that fair ensembles of SFHs for galaxies at these stellar masses are well-described by scale-free, self-similar forms. We also examine their dust attenuation properties and the relationship between nebular and stellar reddening, exploring how these quantities vary with stellar mass and specific SFR (sSFR). Nebular attenuation increases with stellar mass for IMGs but is lower and less mass-dependent in LMGs, consistent with their reduced dust content. In all cases, stellar continuum attenuation is lower than nebular attenuation, as expected from the two-component dust model. The nebular-to-stellar color excess ratio in both samples is consistent with the canonical factor of 2.27. The ratio is mass-independent, but rises with sSFR in IMGs and remains constant in LMGs. These results suggest that in LMGs, efficient dispersal of birth clouds keeps the differential attenuation approximately constant across sSFR. Thus, although LMGs follow the same global SFR– M_* scaling as massive galaxies, their lower dust content and feedback-maintained ISM produce distinct attenuation behavior relative to IMGs.

Keywords: Galaxy formation (595); Dwarf galaxies (416); Galaxy evolution (594); Star formation (1569);

1. INTRODUCTION

Low-mass galaxies (LMGs; $M_* \lesssim 10^9 M_\odot$) are the most numerous systems in the universe. In the early stages of structure formation, galaxies of such masses provided the fundamental building blocks from which larger systems assembled (White & Rees 1978; Dekel & Silk 1986). The low-mass galaxies observed at the present epoch are therefore best understood either as analogs of those primordial systems or as the surviving “leftovers” that have grown slowly and avoided incorpo-

ration into more massive structures. Their abundance in the local universe is well established by the steep low-mass end of the stellar mass function (Baldry et al. 2012). Despite this prevalence, the physical processes governing their evolution remain less well constrained than for more massive galaxies, largely due to observational challenges in obtaining high-quality spectroscopic data for faint systems. Because of their shallow gravitational potentials, LMGs are particularly sensitive to internal feedback from supernovae and stellar winds, as well as to external processes such as ram pressure stripping and tidal interactions. This sensitivity makes them ideal laboratories for studying baryon cycling, star formation regulation, and the enrichment of the circumgalactic and intergalactic media (Tremonti et al. 2004;

Robertson et al. 2010; Peeples & Shankar 2011; Lin et al. 2023).

Star formation in galaxies is commonly parameterized through scaling relations between global properties such as stellar mass (M_*), SFR, and dust content. In massive galaxies, the star-forming main sequence (SFMS) relation between M_* and SFR is well established out to high redshifts, with a slope slightly shallower than unity and modest scatter (e.g., Noeske et al. 2007; Whitaker et al. 2014; Speagle et al. 2014; Kurczynski et al. 2016; Bisigello et al. 2018; Leja et al. 2022). At the low-mass end, the situation is less clear: while several studies find that LMGs largely follow an extrapolation of the SFMS with increased apparent scatter (e.g., Boogaard et al. 2018), much of what is known about SFHs at $M_* \lesssim 10^9 M_\odot$ comes from Local Group/Local Volume dwarfs—systems influenced by the Milky Way–Andromeda environment and not fully representative of the field (Tolstoy et al. 2009; Weisz et al. 2014). Moreover, discrepancies between instantaneous ($H\alpha$) and ~ 100 Myr–averaged (UV/SED) SFR indicators do not uniquely imply discrete “bursts”; similar offsets can arise from smoothly rising SFHs and differences in tracer timescales and associated systematics, as shown by forward modeling of dwarf-galaxy SFHs (Weisz et al. 2012) and recognized in early work on irregulars (Gallagher et al. (1984); see also Lee et al. (2009); Emami et al. (2019); Mehta et al. (2023)). Environmental trends in wide surveys further underscore the need to control for selection when interpreting “burstiness” (Geha et al. 2012).

Dust attenuation is another key parameter shaping our interpretation of galaxy properties, as it affects measurements of SFRs, stellar populations, and emission-line diagnostics. In massive galaxies, the relationship between stellar and nebular attenuation has been extensively studied, with nebular regions generally found to be more obscured than the stellar continuum (Calzetti et al. 2000; Garn & Best 2010; Reddy et al. 2015; Shivaie et al. 2020b; Chartab et al. 2024). This difference is typically interpreted in the framework of a two-component dust model (Charlot & Fall 2000), wherein young stars in H II regions are embedded in dense, dusty birth clouds while the bulk of the stellar light passes through more diffuse ISM dust. Such correlations between nebular-to-stellar reddening and other galaxy properties—such as stellar mass, SFR, sSFR (SFR per unit stellar mass), and gas-phase metallicity—offer valuable insights into dust geometry and the ISM (Garn & Best 2010; Reddy et al. 2015; Hemmati et al. 2015; Shivaie et al. 2020b). However, these studies predominantly focus on massive galaxies, leaving the relationships between dust content,

dust geometry, and other galaxy properties far less explored in low-mass, low-metallicity systems, which are expected to have lower overall dust content, more irregular dust distributions, and potentially different attenuation characteristics.

In this paper, we present a detailed spectroscopic analysis of a statistically significant sample of LMGs at $z \sim 0.15$ in the COSMOS field, based on deep observations with the IMACS spectrograph (Dressler et al. 2011) on the Magellan telescope. We utilize rest-frame optical emission lines to investigate their physical properties, focusing on two key aspects: the star formation rate–stellar mass (SFR– M_*) relation and dust attenuation characteristics, including the differential reddening between nebular and stellar components. We further compare the LMGs to a control sample of intermediate-mass galaxies (IMGs; $10^9 \lesssim M_*/M_\odot \lesssim 10^{10}$) at $z \sim 0.35$, observed with an identical spectroscopic setup (Patel et al. 2023).

The paper is structured as follows: Section 2 describes the sample selection, data and spectroscopic observations. Section 3 outlines our SED fitting and emission-line measurements. Section 4 presents the SFR– M_* relation, dust trends, and nebular-to-stellar reddening ratios. In Section 5, we discuss the implications for feedback, star formation regulation, and dust geometry in LMGs, and summarize our conclusions.

Throughout this paper, we assume a flat Λ CDM cosmology with $H_0 = 70 \text{ kms}^{-1}\text{Mpc}^{-1}$, $\Omega_{m0} = 0.3$, and $\Omega_{\Lambda0} = 0.7$. All the physical parameters are measured assuming a Kroupa (2001) initial mass function (IMF) and the magnitudes are reported on the AB system (Oke & Gunn 1983).

2. DATA

In this paper, we study a sample of LMGs in the Cosmic Evolution Survey (COSMOS; Scoville et al. 2007) field. Our galaxies are initially selected based on two criteria on their stellar mass and photometric redshift (z_{phot}):

1. $10^8 \leq M_*/M_\odot \leq 10^9$;
2. $0.1 \leq z_{phot} \leq 0.2$.

Spectroscopy of these galaxies was acquired in 2019, 2023, and 2024. We discuss details of the observations in the next section. The galaxies observed in 2019 were selected from Muzzin et al. (2013a), with their z_{phot} calculated using the EAZY code (Brammer et al. 2008) and their stellar masses determined through the SED fitting code of FAST (Kriek et al. 2009). However, the more recent sample was selected from the CLASSIC cat-

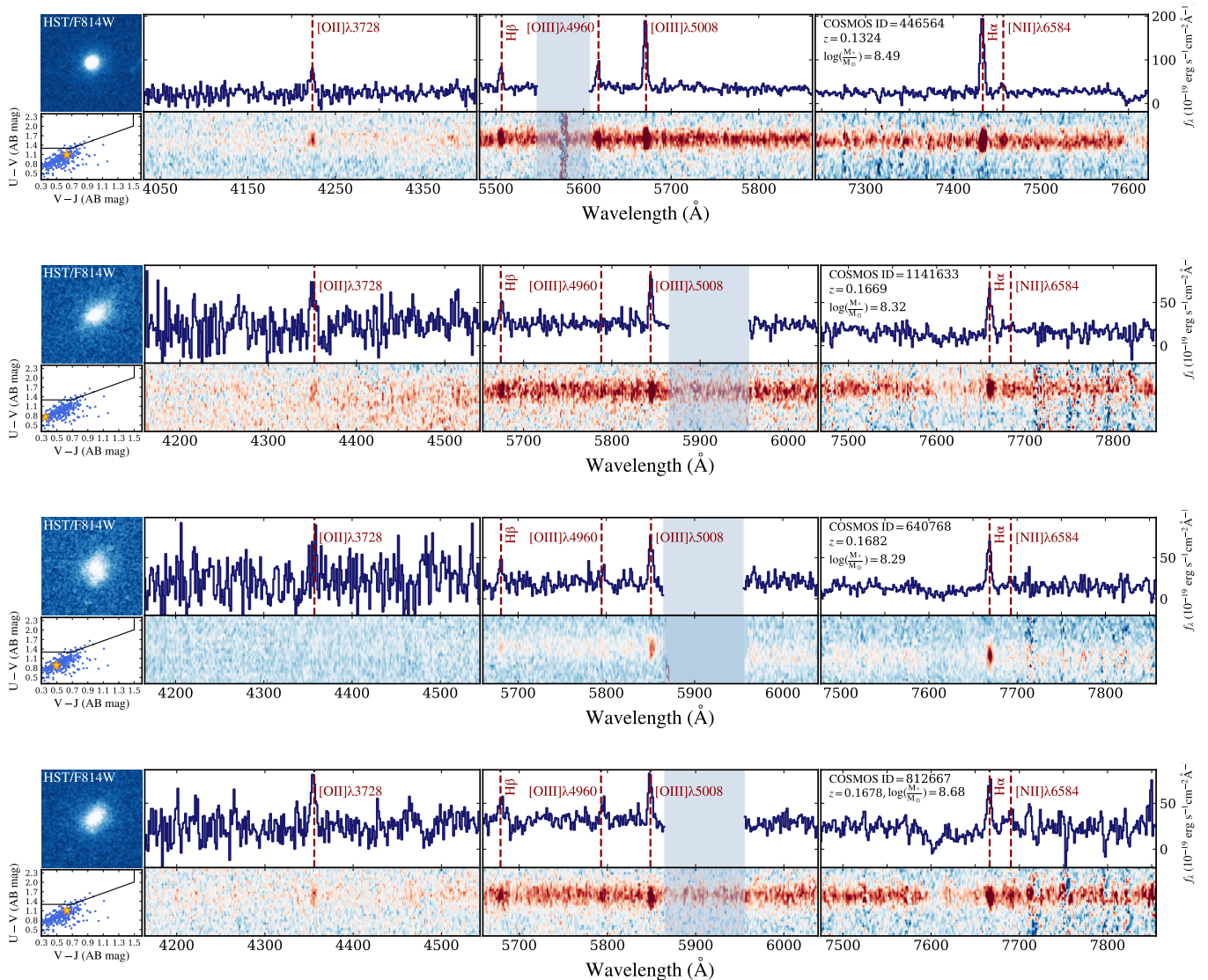


Figure 1. 1D and 2D observed-frame spectra of four example LMGs observed with a ~ 3.5 -hour exposure using IMACS/Magellan. In each row, the UVJ diagram (bottom left) displays the entire sample of LMGs with the example galaxy marked (yellow star). The F814W/HST cutout of the galaxy is also shown in the top left.

alog of COSMOS2020 (Weaver et al. 2022). The stellar mass and z_{phot} of these sources are selected from a combination of EAZY (Brammer et al. 2008) and LePhare (Arnouts et al. 2002; Ilbert et al. 2006) solutions of SED fitting.

For all the sources initially selected from the two catalogs of Muzzin et al. (2013a) and Weaver et al. (2022) based on their stellar mass and z_{phot} , we then perform SED fitting by fixing their redshifts to the spectroscopic values to recalculate their physical properties (Section 3.1).

2.1. IMACS Observations

Deep optical spectroscopic observation of our galaxies is obtained using the Inamori-Magellan Areal Camera

and Spectrograph (IMACS; Dressler et al. 2011) at the Magellan Baade telescope over the observing programs during 2019, 2023, and 2024. All 12 masks were observed under clear conditions with an average seeing of $\sim 0.6''$. The typical exposure time for each mask was ~ 210 minutes.

$f/2$ spectroscopy with 300 mm^{-1} grism disperser and the appropriate spectroscopic filter was used in all runs, yielding a spectral resolving power of $R \sim 1000$ (resolving $\sim 6 \text{ \AA}$ at 6000 \AA). The slit widths were $1''$, which corresponds to $1.84\text{--}3.30 \text{ kpc}$ across $0.1 \leq z \leq 0.2$ (2.61 kpc at $z = 0.15$) and $4.45\text{--}5.37 \text{ kpc}$ across $0.3 \leq z \leq 0.4$ (4.94 kpc at $z = 0.35$). The wide range of wavelength coverage ($3700\text{--}9500 \text{ \AA}$) allows the detection

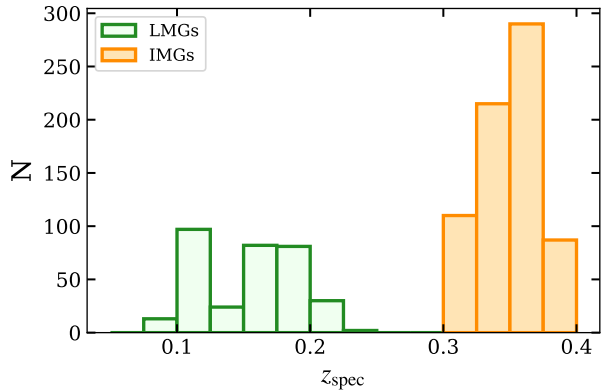


Figure 2. Spectroscopic redshift distribution of both LMGs and IMGs.

of strong emission lines, such as $H\alpha$ and $H\beta$, simultaneously.

2.2. Data Reduction

To reduce the spectroscopic data, we utilize the Carnegie Python Distribution (CarPy¹), which is a powerful tool tailored for IMACS observations (see e.g., Kelson et al. 2000; Kelson 2003). The pipeline stacks individual frames, subtracts the sky background, rectifies and extracts 2D spectra. Following this, we apply the optimal extraction algorithm to obtain 1D spectra of galaxies and associated errors (e.g., Horne 1986). Spectroscopic redshifts of galaxies are determined based on strong emission lines in the galaxy spectra, such as $H\alpha$, $[\text{OIII}]\lambda 5008$, and $[\text{OI}]\lambda 3727$. Figure 1 displays both 2D and 1D spectra for selected LMGs, along with their positions on the UVJ diagram and their F814W/HST postage stamps.

2.3. Intermediate-Mass Control Sample

As a comparison, a similarly observed sample of IMGs is also added to our LMG sample. The details of the observation and sample selection of these galaxies are discussed extensively in Patel et al. (2023), but we provide a brief summary here. IMGs had been initially selected from Muzzin et al. (2013a) based on their z_{phot} and stellar mass, such that $10^9 \leq M_*/M_\odot \leq 10^{10}$, and $0.3 \leq z_{\text{phot}} \leq 0.4$. The stellar masses were the product of FAST SED fitting code (Kriek et al. 2009), and the photometric redshifts were measured with the EAZY code (Brammer et al. 2008). Magellan IMACS spectroscopy, along with the measurement of spectroscopic redshifts and emission line fluxes, is detailed in Patel

et al. (2023). For a full description, we refer the reader to this work.

Figure 2 shows the spectroscopic redshift distribution for both LMG and IMG samples. Our main sample consists of 329 LMGs (green histogram) and 702 IMGs (orange histogram) at $0.1 \lesssim z \lesssim 0.2$ and $0.3 \lesssim z \lesssim 0.4$, respectively.

3. ANALYSIS

3.1. SED Fitting

Utilizing the Bayesian Analysis of Galaxies for Physical Inference and Parameter ESTimation (Bagpipes; Carnall et al. 2018)² framework, we fit the UV to mid-infrared SEDs of both LMGs and IMGs to derive their physical properties, and to model the high resolution spectrum of Balmer absorption underneath the emission lines. The observed photometry for these galaxies is taken from the COSMOS2020 CLASSIC catalog (Weaver et al. 2022), which is corrected for galactic dust and rescaled to the total flux for the 3'' diameter aperture photometry. The SED fitting uses broad-band photometry spanning GALEX NUV; CFHT u ; Subaru/HSC g , r , i , z , y ; UltraVISTA Y , J , H , K_s ; and Spitzer/IRAC channels 1 and 2 (3.6 and 4.5 μm).

We adopt photometry from the COSMOS2020 CLASSIC catalog rather than the FARMER catalog. For the optical magnitude range of our sample (HSC $i \sim 20\text{--}23$ AB), we find that CLASSIC and FARMER broad-band fluxes are highly consistent for all photometric bands used in the SED fitting. As a result, the choice of photometric catalog does not significantly affect the results/conclusions of our analysis. In addition, CLASSIC aperture photometry is particularly robust for LMGs with irregular, clumpy, or asymmetric morphologies, which are common among our sample.

Bagpipes employs the 2016 version of the Bruzual & Charlot (2003) stellar population synthesis (SPS) models. Additionally, the nebular emission modeling within the code utilizes the 2017 version of the Cloudy photoionization code (Ferland et al. 2017) based on the Byler et al. (2017) methodology. In the process of SED fitting, we fix the redshifts to their spectroscopic values and adopt a delayed exponentially declining SFH of the form $t e^{-t/\tau}$. We impose a uniform prior on the star formation e-folding time-scale (τ), ranging from 0.3 to 10 Gyr. For dust attenuation, we adopt the Calzetti et al. (2000) attenuation curve with $A_V \in (0, 2)$ for the IMG sample. For LMGs, we instead employ the Small Magellanic Cloud (SMC) extinction curve (Gordon et al.

¹ <https://code.obs.carnegiescience.edu/>

² <https://bagpipes.readthedocs.io/en/latest/>

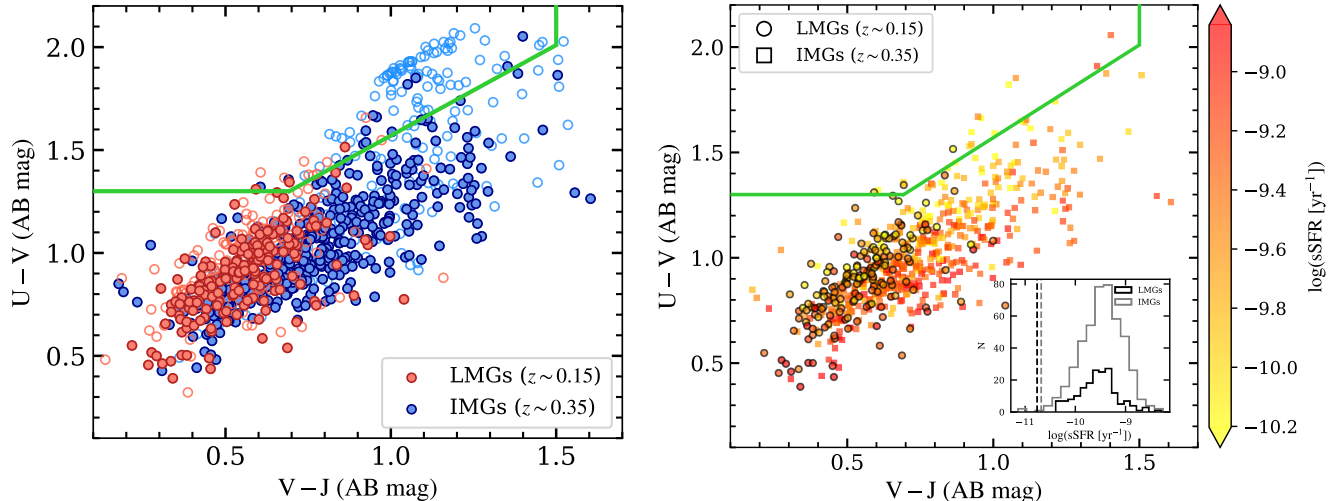


Figure 3. *Left:* The rest-frame UVJ plane derived from SED fitting for both LMGs (red) and IMGs (blue). The filled red (blue) colors correspond to LMGs (IMGs) with 3σ detection in their $H\alpha$ and $H\beta$ lines. The green line indicates the boundary between quiescent galaxies and star-forming galaxies. *Right:* The same galaxies shown in the left panel, limited to objects with $\geq 3\sigma$ detections in both $H\alpha$ and $H\beta$, color-coded by their sSFR. The inset shows the sSFR distributions of the LMG and IMG samples, with the vertical dashed line indicating the star-forming/quiescent division at $\text{sSFR} = 0.2/t_U(z)$ evaluated at the median redshift of each sample.

2003), motivated by observational and theoretical studies showing that SMC-like dust laws provide a better description of low-metallicity, low-mass systems (e.g., Salmon et al. 2016; Reddy et al. 2018; Salim et al. 2018; Shivaie et al. 2020b). Additionally, we allow the stellar metallicity to vary over the range $0 < Z/Z_\odot < 2.5$, assuming a logarithmic prior.

The best-fit SED model for each galaxy, along with stellar masses and other physical parameters (e.g., SFR and stellar dust attenuation), is obtained from SED fitting. The rest-frame UVJ colors are also measured for both LMGs and IMGs. In the left panel of Figure 3, we demonstrate the position of our galaxies on the rest-frame UVJ plane. The green line in the figure separates the population of quiescent galaxies from the star-forming ones based on the definition from Muzzin et al. (2013b). The filled red (blue) data points correspond to LMGs (IMGs) with 3σ detections in their $H\alpha$ and $H\beta$ lines used in the present work.

As shown in the figure, the vast majority of our LMGs and IMGs lie in the star-forming region of the UVJ plane, with only a small minority ($\sim 1\%$ of LMGs and $\sim 2\%$ of IMGs) classified as quiescent. We exclude these quiescent galaxies from both samples. Adopting an sSFR-based criterion (Pacifci et al. 2016), $\text{sSFR} > 0.2/t_U(z)$ (where $\text{sSFR} \equiv \text{SFR}_{H\alpha}/M_*^{\text{SED}}$ and $t_U(z)$ is the age of the Universe at redshift z), yields a relatively consistent classification, with disagreements limited to

a few objects ($\lesssim 2\%$) in the total sample, as illustrated by the sSFR distribution in the right panel of Figure 3.

We note that UVJ-based classifications are known to be imperfect, with potential contamination from dusty star-forming galaxies near the quiescent boundary (Leja et al. 2019). However, in the present analysis, this effect is minimal given the consistency between UVJ- and sSFR-based classifications.

3.2. Emission Line Measurements

Given the wide wavelength coverage of IMACS, we measure the emission line fluxes in three wavelength ranges with strong emission lines:

1. $[\text{OII}]\lambda\lambda 3727, 3730$;
2. $H\beta$, $[\text{OIII}]\lambda\lambda 4960, 5008$;
3. $H\alpha$, $[\text{NII}]\lambda\lambda 6550, 6585$.

In each wavelength range, we simultaneously fit multiple Gaussians to the 1D spectra of galaxies to extract the desired emission line fluxes. The fluxes of $H\alpha$ and $H\beta$ emission lines are corrected for underlying Balmer absorption using the best-fit SED models obtained in Section 3.1. We measure the line fluxes by integrating the best-fit Gaussian function over the 1D spectrum. Uncertainties are taken from the covariance matrix of the multi-Gaussian fit, with continuum and per-pixel variance propagated to the integrated line flux.

4. RESULTS

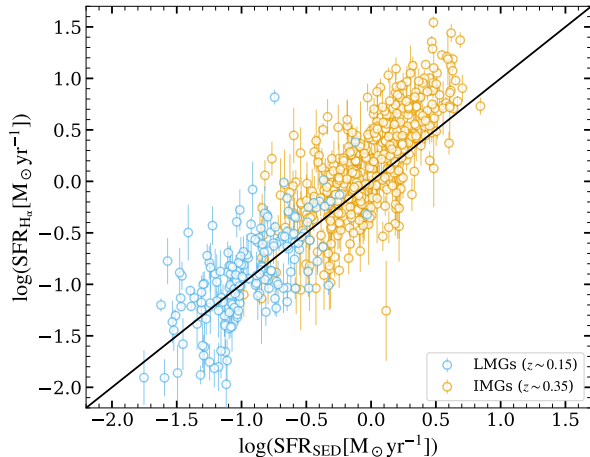


Figure 4. Comparison between the SFRs estimated from SED fitting (SFR_{SED}) with those based on the $\text{H}\alpha$ luminosity ($\text{SFR}_{\text{H}\alpha}$) for LMGs (blue circles) and IMGs (orange circles). The black line represents a unit slope, indicating equality between $\text{SFR}_{\text{H}\alpha}$ and SFR_{SED} .

4.1. $\text{SFR}-M_*$ Relation

Out of 329 (702) LMGs (IMGs) at $z \sim 0.15$ ($z \sim 0.35$), 174 (448) of them have signal-to-noise (S/N) ≥ 3 detection in their $\text{H}\alpha$ and $\text{H}\beta$ emission lines (these galaxies are shown with bold colors on the UVJ diagram in the left panel of Figure 3). We derive the $\text{H}\alpha$ -based SFRs ($\text{SFR}_{\text{H}\alpha}$) for our LMG and IMG samples using the Kennicutt (1998) calibration for a Kroupa (2001) IMF: $\text{SFR}_{\text{H}\alpha} (M_{\odot} \text{ yr}^{-1}) = 5.5 \times 10^{-42} L_{\text{H}\alpha} (\text{erg/s})$. $\text{H}\alpha$ fluxes used for the SFR measurements are corrected for attenuation using the Balmer decrement (see Section 4.2). Uncertainties on $\text{SFR}_{\text{H}\alpha}$ include both line-flux measurement errors and propagated $E(B-V)_{\text{neb}}$ uncertainties.

We also estimate SFRs from SED fitting (SFR_{SED}). While the SFR coming from $\text{H}\alpha$ flux measurements traces the instantaneous star formation activity within galaxies, the SED-derived SFR is the integrated SFR of the galaxy over 100 Myrs and is more susceptible to degeneracies present in SED modeling. Nevertheless, as shown in Figure 4, both indicators are in reasonable agreement, with a normalized median absolute deviation (σ_{NMAD}) of ~ 0.3 for each sample, consistent with the results of Patel et al. (2023) for IMGs. As an external benchmark on short-timescale variability for IMGs, Patel et al. (2023) compared dust-corrected $\text{H}\alpha$ and rest-frame 2800 Å UV luminosities and found a very small intrinsic scatter between their offsets from the respective sequences ($\sigma_{\delta} \lesssim 0.03$ dex), which limits recent SFR variability to $\lesssim 2$ over 200 Myr and $\lesssim 30\%$ over 20 Myr—disfavoring strongly bursty SFHs and favoring an ensemble of gently varying histories. This behavior is naturally connected to the dependence of nebular atten-

uation on sSFR, which we examine explicitly in Section 4.2 and Figure 8.

Figure 5 presents the relation between $\text{SFR}_{\text{H}\alpha}$ and stellar mass for LMGs and IMGs. Following Kelson (2014), we assume that the median sSFR declines as the inverse of cosmic time, $\langle \text{sSFR} \rangle \propto 1/t_U(z)$, which implies a mass-independent evolution in the normalization of the SFMS. Under our assumed cosmology, this corresponds to a ~ 0.08 dex decrease in $\log(\text{SFR})$ from $z \sim 0.35$ to $z \sim 0.15$, so we shift the higher- z sample (IMGs) by -0.08 dex to place both samples on a common ($z \sim 0.15$) evolutionary frame.

We model the SFMS as a linear relation in log space, $\log(\text{SFR}_{\text{H}\alpha}) = a \log(M_*/M_{\odot}) + b$. Parameters (a, b) are obtained by ordinary least squares (minimizing vertical residuals) using `curve_fit` (Virtanen et al. 2020). To obtain robust uncertainties on (a, b), we employ bootstrap resampling; we draw 1000 samples with replacement from the combined (LMGs + shifted IMGs) dataset, refit the linear relation to each realization, and report the median slope and intercept along with their 16th–84th percentile ranges. The shaded band in Figure 5 shows the 68% confidence region derived from the distribution of bootstrap regression lines. The regression uses only objects with $\text{S/N} \geq 3$ in both $\text{H}\alpha$ and $\text{H}\beta$; we do not incorporate the S/N selection cuts into the fit. Instead, we indicate “representative” $\text{S/N} \geq 3$ detection floors in the $\text{SFR}-M_*$ plane (horizontal gray dashed lines in each mass range), computed from the median 1σ line-flux depths and median nebular A_V for each sample (and shifted by -0.08 dex for IMGs to match the joint-fit frame).

A single linear fit to the combined sample (purple line) yields a slope of 1.01 ± 0.03 and intercept -9.66 ± 0.30 in the $z \sim 0.15$ frame, i.e., SFR increases systematically with stellar mass in all mass ranges, following the expected SFMS trend (e.g., Speagle et al. 2014). We estimate the intrinsic scatter of $\sigma_{\text{int}} \sim 0.4$ dex, which is identical to the expectation for an $\text{H} = 1$ stochastic process and scale-free gravitational collapse (Kelson 2014; Kelson et al. 2020).

For comparison, Figure 5 also overlays other relations from literature as reference. We plot the SAGA dwarfs best-fit line from Geha et al. (2024) (light-green dotted), which anchors the low-mass, low- z regime, and the constant-sSFR guide from Kelson (2014) evaluated at $z = 0.15$ (red dot-dashed). We further show the time-evolving “consensus” main sequence from Speagle et al. (2014) evaluated at our sample redshift (orange dotted). As a theoretical check, we include the FIRE zoom-in locus at $z = 0$ from Sparre et al. (2017) (green dashed). In FIRE, the ensemble FUV-based main se-

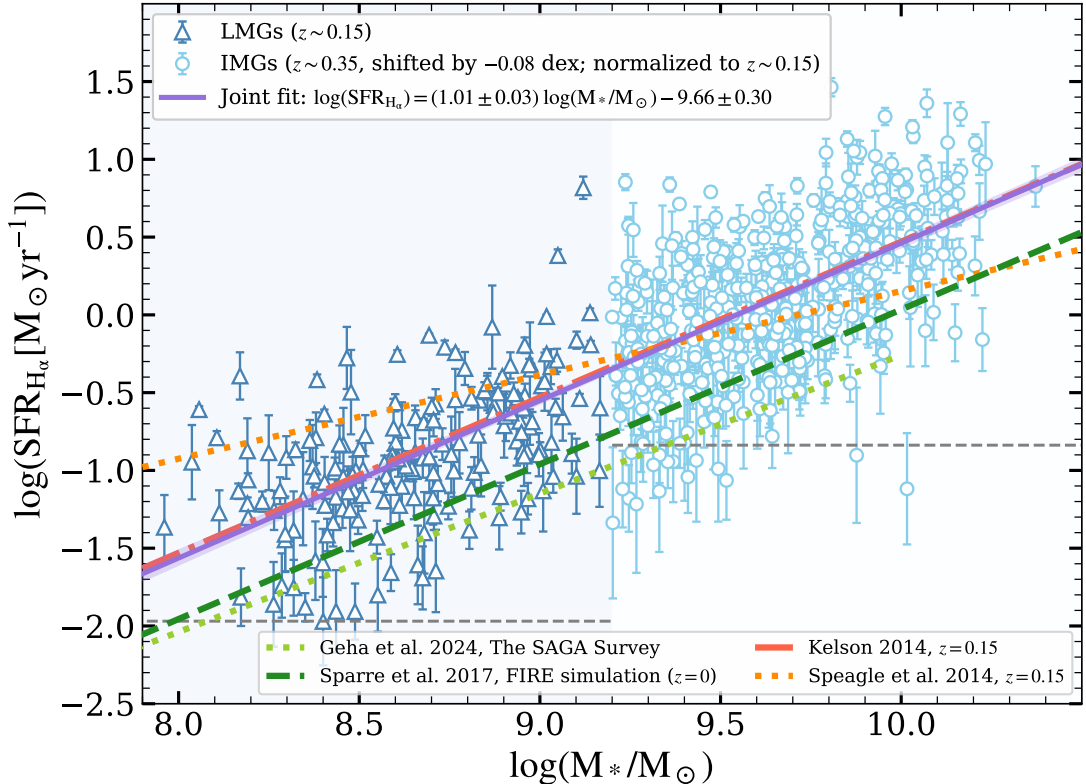


Figure 5. $\text{SFR}_{\text{H}\alpha}$ - M_* relation for LMGs and IMGs. Blue triangles show LMGs ($z \sim 0.15$) and light-blue circles show IMGs shifted by -0.08 dex in $\log(\text{SFR})$ to the $z \sim 0.15$ frame. The solid purple line is the joint fit (ordinary least squares on $\log \text{SFR}_{\text{H}\alpha}$ vs. $\log M_*$), yielding $b = 1.01 \pm 0.03$ and intercept -9.66 ± 0.30 ; the shaded envelope indicates the 68% confidence interval from 1000 bootstrap realizations. For context we overlay other relations from literature: Speagle et al. (2014) at $z = 0.15$ (orange dotted), the constant-sSFR track from Kelson (2014) at $z = 0.15$ (red dash-dot), the SAGA dwarfs line from Geha et al. (2024) (green dotted), and the FIRE zoom-in locus from Sparre et al. (2017) at $z = 0$ (dark green dashed). Gray dashed horizontal segments indicate the representative $\text{S/N} \geq 3$ detection floors; the IMG threshold is shown with the same -0.08 dex shift for consistency. Error bars on points denote 1σ uncertainties in $\log(\text{SFR}_{\text{H}\alpha})$.

quence has an approximately unity slope over our mass range, but the $\text{H}\alpha$ -based SFRs on ~ 10 Myr timescales exhibit larger variability, especially below $M_* \sim 10^{10} M_\odot$, indicative of bursty SFHs. By contrast, our observed intrinsic scatter of $\sigma_{\text{int}} \sim 0.4$ dex is comparable in both mass ranges and aligns with previous observational constraints for massive galaxies (e.g., Kurczynski et al. 2016). Thus, if one infers SFH “burstiness” from the SFMS scatter alone, our LMGs exhibit variations similar to those of more massive star-forming systems.

We emphasize that the SED fitting in this work is not used to infer SFHs. The delayed exponentially declining SFH adopted in the SED fitting is chosen to provide robust stellar masses, stellar continuum attenuation, and Balmer absorption corrections, rather than to recover time-resolved SFHs. Previous studies have shown that stellar mass estimates are relatively insensitive to SED fitting assumptions (Pacifi et al. 2023). As a result, our discussion of bursty versus smoothly varying star formation does not rely on the SED-based SFH itself.

Instead, constraints on burstiness are based on spectroscopic diagnostics, including the scatter in the $\text{SFR}-M_*$ relation (SFMS) derived from $\text{H}\alpha$ -based SFRs.

Finally, Figure 6 compiles the comparison measurements of the SFMS slope as a function of redshift from the literature; the legend indicates the SFR indicator adopted along with the stellar mass range in each study. At very low redshift, we include the SDSS analysis of Renzini & Peng (2015), who define the SFMS as the ridge line of the three-dimensional (SFR , M_* , number) distribution over $0.02 < z < 0.085$. At $0.1 < z < 0.5$, we show the VLT/MUSE results of Boogaard et al. (2018), who derive dust-corrected $\text{H}\alpha$ -based SFRs via the Balmer decrement for LMGs and fit the MS slope across $\sim 10^7$ - $10^{10.5} M_\odot$. For $0.5 < z < 1$, we plot determinations from Whitaker et al. (2014) (based on a mass-complete 3D-HST/CANDELS sample with UV+IR SFRs), Kurczynski et al. (2016) (hierarchical fits to SED-based SFRs allowing for intrinsic scatter), and Bisigello et al. (2018) (UV with

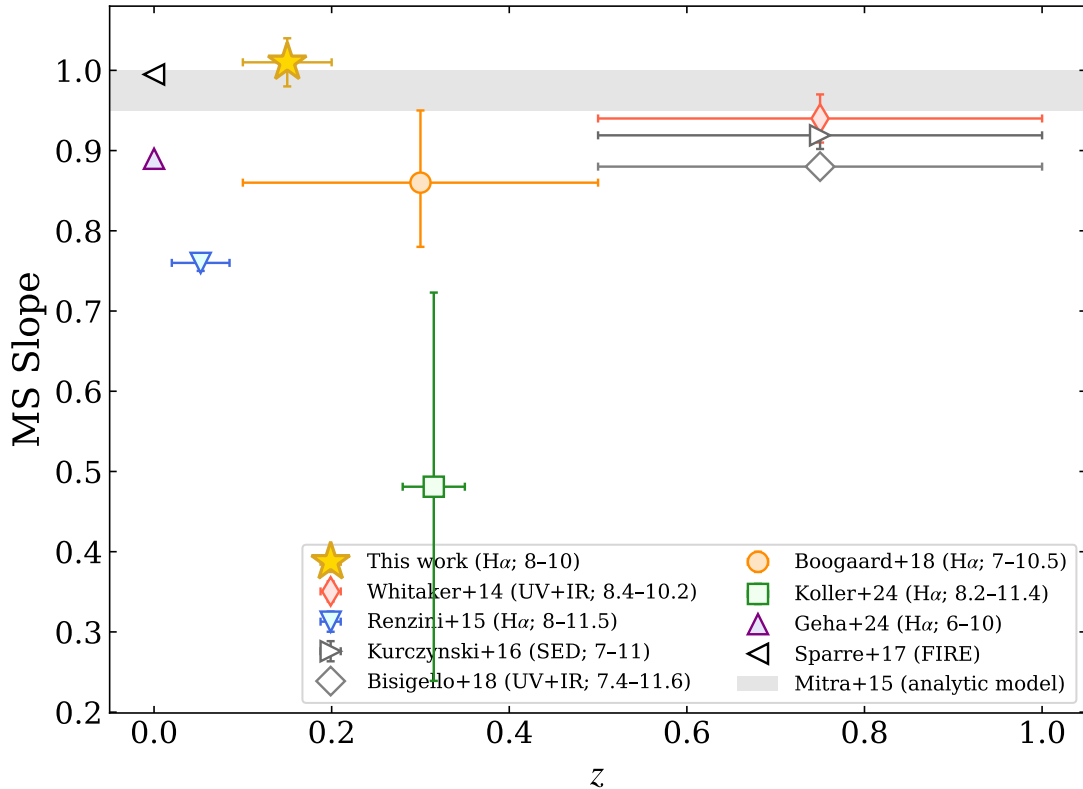


Figure 6. Slope of the SFMS as a function of redshift, where the MS slope a is defined by $\log(\text{SFR}) = a \log(M_*/M_\odot) + b$. The gold star marks this work (joint fit to LMGs and IMGs), yielding $a = 1.01 \pm 0.03$ at $z \sim 0.15$. Literature points (symbols/labels) include Whitaker et al. (2014) (UV+IR), Renzini & Peng (2015) (H α), Kurczynski et al. (2016) (SED), Bisigello et al. (2018) (UV+IR), Boogaard et al. (2018) (H α), Koller et al. (2024) (H α), Geha et al. (2024) (H α), and the FIRE zoom-ins from Sparre et al. (2017). Horizontal bars indicate each study’s redshift range; vertical bars show the reported 1σ uncertainty on a . The gray band denotes the analytic expectation for the SFMS (i.e., $a \sim 1$) from Mitra et al. (2015). Numbers in the legend denote the stellar-mass interval (in $\log(M_*/M_\odot)$) over which each slope was measured.

mid/far-IR constraints in CANDELS/GOODS-S). We also show MAGPI IFS results from Koller et al. (2024) at $0.28 < z < 0.35$, noting that their global (integrated) MS slope is less tightly constrained than their resolved rSFMS measurements. As additional anchors, we include the FIRE hydrodynamical prediction at $z \sim 0$ (Sparre et al. 2017) and the SAGA survey result for nearby satellites (Geha et al. 2024). The gray band denotes the slope range from the analytic equilibrium model of Mitra et al. (2015).

Our measured MS slope is consistent with the \sim unity value in the FIRE simulations (Sparre et al. 2017) and with the analytic expectations of Mitra et al. (2015); it also agrees with the Whitaker et al. (2014) slope value despite that study’s higher redshift. A slope consistent with unity in the SFMS implies an approximately mass-invariant sSFR over the fitted mass range ($\text{SFR} \propto M_*$). This indicates that galaxies in this stellar mass range grow their stellar content in a self-similar manner, form-

ing stars at rates directly proportional to their existing stellar mass.

We note that several literature studies shown extend to stellar masses well above the range probed here, where a turnover or flattening of the SFMS is often observed; slopes reported over broader mass ranges may therefore differ systematically from those measured when restricting the fit to lower stellar masses.

4.2. Dust Attenuation

We estimate the nebular dust attenuation for both LMGs and IMGs using the Balmer decrement, defined as the H α /H β line flux ratio. An intrinsic ratio of 2.86 is adopted, corresponding to case B recombination under typical conditions of $T = 10^4$ K and $n_e = 10^2 \text{ cm}^{-3}$ (Osterbrock & Ferland 2006). To convert the color excess to attenuation ($A_\lambda = k_\lambda E(B-V)$), we apply the Calzetti et al. (2000) attenuation curve for IMGs, while for LMGs we adopt the SMC extinction curve from Gordon et al. (2003), in line with their lower metallicities and the evidence that SMC-like dust laws better charac-

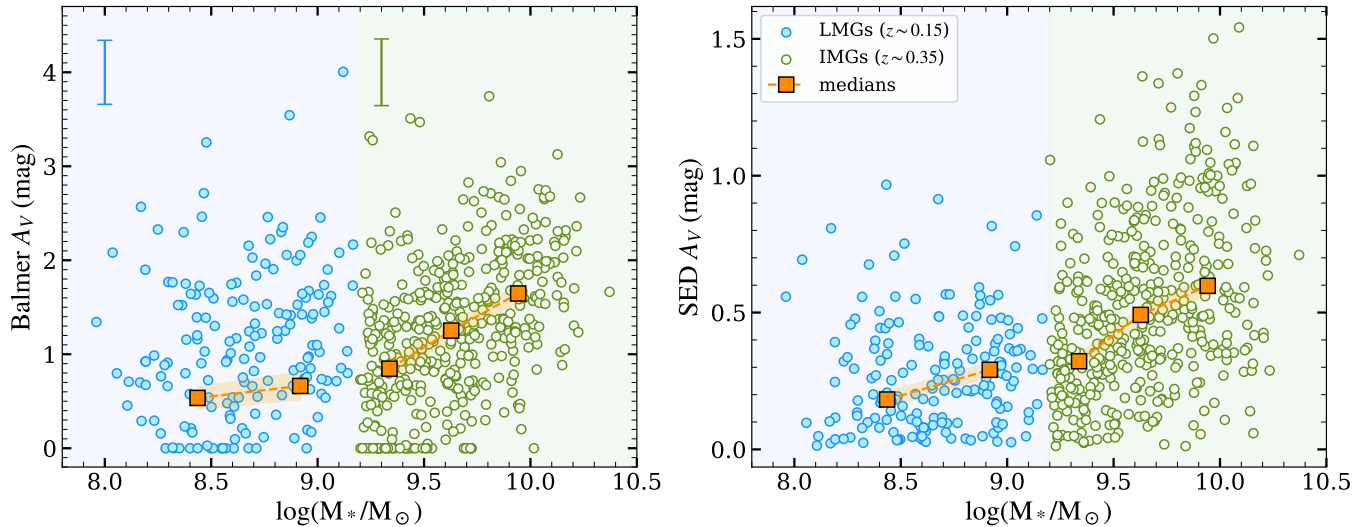


Figure 7. Left: Balmer A_V plotted against stellar mass for LMGs (blue circles) and IMGs (green circles). Orange squares indicate the median trend within each sample. The typical error bar of each sample is displayed in the top-left corner. Right: SED-derived A_V versus stellar mass for LMGs (blue circles) and IMGs (green circles), with the median trend shown as orange squares across different stellar mass bins. The shaded regions around the median values in each panel indicate the uncertainty associated with these medians.

terize such systems (e.g., Salim et al. 2018; Shivaie et al. 2020a). Uncertainties in attenuation are computed by propagating the flux errors on $H\alpha$ and $H\beta$ using standard error propagation techniques. When the measured Balmer decrement is consistent with or below the intrinsic Case B value within uncertainties, the inferred $E(B-V)_{\text{nebular}}$ would be formally negative; in such cases we set $E(B-V)_{\text{nebular}} = 0$ (and hence $A_V = 0$), as negative attenuations are unphysical.

4.2.1. Trends in Nebular and Stellar Attenuation

The left panel of Figure 7 shows Balmer A_V as a function of stellar mass for LMGs and IMGs, with medians in stellar mass bins indicated by orange squares. To compute these medians, we use an inverse-variance-weighted method (Edgeworth 1888) that accounts for non-uniform measurement uncertainties in the Balmer decrement. Specifically, within each mass bin we sort the A_V values, accumulate their normalized weights, and define the median as the value at which the cumulative weight first reaches 0.5. The uncertainty on each median is estimated from the weighted scatter of the points in the bin, adjusted by the effective sample size.

IMGs exhibit a clear increase in Balmer A_V with stellar mass, consistent with previous studies of the mass-attenuation relation at both low and high redshifts (e.g., Garn & Best 2010; Cullen et al. 2018). In contrast, LMGs show systematically lower A_V values and a markedly weaker dependence on stellar mass. This aligns with the known dust deficiency of low-mass, low-

metallicity galaxies (e.g., Rémy-Ruyer et al. 2014; De Vis et al. 2019), which exhibit low dust-to-gas ratios, steeper attenuation curves, and reduced overall attenuation (Reddy et al. 2018; Shivaie et al. 2020b; Salim & Narayanan 2020). The mass-independence of A_V in LMGs likely reflects fundamental limits on dust production and retention in the low-metallicity, feedback-dominated environments of dwarf galaxies.

A forthcoming analysis of gas-phase metallicities in these LMGs will provide direct constraints on their chemical enrichment and enable a quantitative link among metallicity, dust content, and attenuation; in parallel, morphological measurements from HST/JWST imaging will place these relations in structural context, providing a better understanding of the predominance of local dust around the HII regions versus the broad interstellar dust distributions within these galaxies.

The right panel of Figure 7 shows the stellar continuum attenuation (SED A_V) from our SED fitting as a function of stellar mass, with median values in stellar mass bins again shown by orange squares. In both LMGs and IMGs, SED A_V increases with stellar mass. However, at fixed stellar mass, SED A_V is systematically lower than the nebular A_V , in agreement with previous findings that nebular regions experience higher dust attenuation than the stellar continuum (e.g., Calzetti et al. 2000; Garn & Best 2010; Hemmati et al. 2015; Qin et al. 2019; Shivaie et al. 2020b; Patel et al. 2023; Chartab et al. 2024). For the IMG sample, these analyses are also reported in Patel et al. (2023), and our measurements are consistent with theirs.

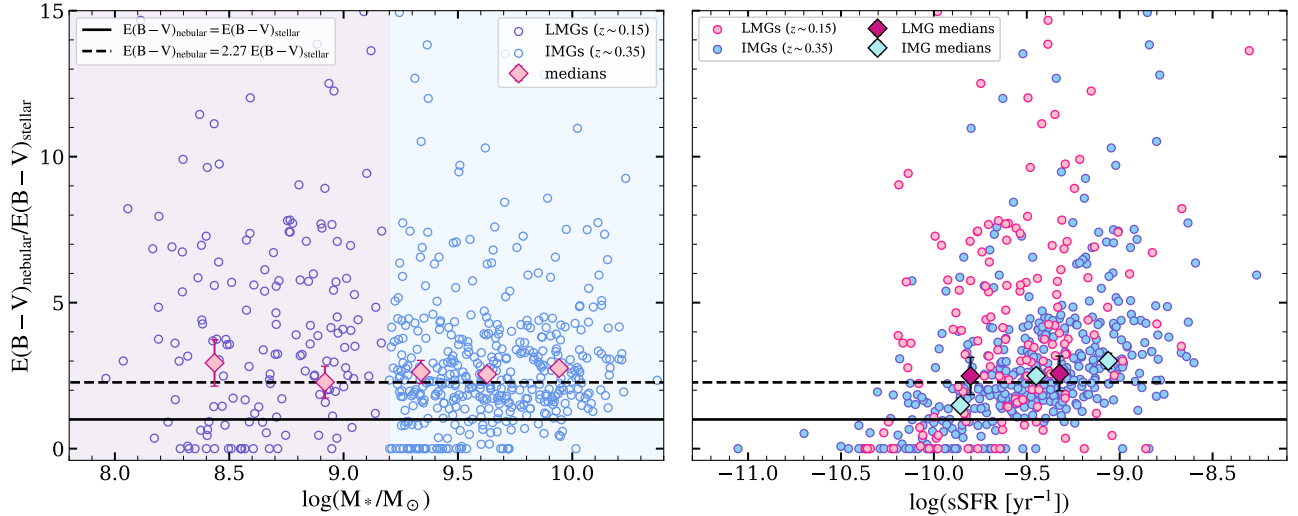


Figure 8. Left: Variation of nebular to stellar color excess with stellar mass for LMGs (purple circles) and IMGs (blue circles). Median values for each sample are represented in two stellar mass bins using pink diamonds. Error bars indicate the uncertainty of these medians. Right: Nebular to stellar color excess as a function of sSFR for LMGs (pink circles) and IMGs (blue circles). Median values, along with their uncertainties, are depicted with magenta (blue) diamonds for the LMG (IMG) sample in two bins of sSFR. The solid and dashed lines in both panels show identical nebular and stellar color excess, and the relation between the two reddening from Calzetti et al. (2000) ($E(B - V)_{\text{nebular}} = 2.27 E(B - V)_{\text{stellar}}$), respectively.

4.2.2. Nebular-to-Stellar Reddening Ratios

To further investigate the differential attenuation in our samples, we plot $E(B - V)_{\text{nebular}}/E(B - V)_{\text{stellar}}$ as a function of stellar mass in the left panel of Figure 8. Median values in stellar mass bins for each sample are shown as pink diamonds. The solid horizontal line corresponds to equal reddening of nebular and stellar components, while the dashed line marks the canonical $E(B - V)_{\text{nebular}} = 2.27 E(B - V)_{\text{stellar}}$ relation for local starbursts (Calzetti et al. 2000).

For both samples the median ratios lie close to this canonical value, in agreement with previous studies of galaxies at similar masses and redshifts (e.g., Kashino et al. 2013; Price et al. 2014; Shivaie et al. 2020b). Also, there is no statistically significant correlation between the reddening ratio and stellar mass within either population, consistent with earlier findings for more massive systems (e.g., Hemmati et al. 2015; Reddy et al. 2015; Shivaie et al. 2020b).

We also examine the dependence of the nebular-to-stellar color excess ratio on sSFR in the right panel of Figure 8. The sSFR is derived from the dust-corrected $H\alpha$ SFR ($\text{SFR}_{H\alpha}$), as described in Section 4.1. The solid and dashed horizontal lines indicate equal reddening for the nebular and stellar components and the Calzetti et al. (2000) relation ($E(B - V)_{\text{neb}} = 2.27 E(B - V)_{\text{star}}$), respectively. Median values in bins of sSFR are shown as magenta (LMGs) and blue (IMGs) diamonds, with error bars indicating the uncertainty on the median.

At low sSFR ($\sim 10^{-10} \text{ yr}^{-1}$), LMGs exhibit a relatively elevated nebular-to-stellar attenuation ratio compared to IMGs, but the median value remains flat as sSFR increases. This flatness contrasts with the clear positive correlation observed in IMGs. A possible interpretation is that, in LMGs, short birth-cloud clearing times at high sSFR prevents long-lived obscuration (e.g., Chevance et al. 2020). By contrast, the deeper potential wells and higher dust masses of IMGs allow H II regions to remain optically thick as sSFR increases, producing a strong sSFR-dependent rise in the nebular-to-stellar ratio. This possible rise at higher sSFR is qualitatively consistent with results for high-redshift star-forming galaxies (e.g., Reddy et al. 2015; Shivaie et al. 2020b), and may reflect dust geometries in which the youngest, most strongly star-forming regions are more heavily embedded in dust than the older stellar populations.

This sSFR-dependent increase in nebular attenuation provides a natural physical explanation for the offset between $\text{SFR}_{H\alpha}$ and SFR_{SED} observed at high SFR in Figure 4. As sSFR increases, particularly for IMGs, star-forming regions become increasingly embedded and optically thick, enhancing the attenuation of nebular emission relative to the stellar continuum. We emphasize that this behavior reflects changes in dust geometry and the embedding of H II regions at fixed star formation activity, rather than strongly bursty SFHs, which are independently constrained to be relatively smooth on short timescales for IMGs (Patel et al. 2023).

5. DISCUSSION & SUMMARY

In this paper, we have presented a detailed spectroscopic analysis of low-mass galaxies (LMGs; $M_* \lesssim 10^9 M_\odot$) at $z \sim 0.15$ in the COSMOS field, based on deep IMACS/Magellan observations, and compared them to a control sample of intermediate-mass galaxies (IMGs; $10^9 \lesssim M_*/M_\odot \lesssim 10^{10}$) at $z \sim 0.35$ observed with the same instrumental setup. The final sample includes 174 LMGs and 448 IMGs with $\geq 3\sigma$ detections in both H α and H β . Using photometry from the COSMOS2020 CLASSIC catalog and fixing redshifts to their spectroscopic values, we performed SED fitting with `Bagpipes` to derive stellar masses, stellar dust attenuation, and other physical parameters. Our main findings are summarized below.

- We measured H α -based SFRs (dust-corrected via the Balmer decrement) and compared them to SED-based SFRs, finding good agreement ($\sigma_{\text{NMAD}} \sim 0.3$). In the SFR- M_* plane, we fit a single linear relation to LMGs and IMGs. The joint ordinary-least-squares fit yields a slope of $a = 1.01 \pm 0.03$ and intercept $b = -9.66 \pm 0.30$, consistent with an approximately linear SFMS at these masses and redshifts. The inferred intrinsic scatter is $\sigma_{\text{int}} \sim 0.4$ dex across the full mass range. Both the near-unity SFMS slope and the modest intrinsic scatter point to gradual, scale-free stellar-mass assembly, with no evidence that LMGs are systematically more bursty than IMGs. The comparable scatter in both samples indicates that low-mass systems build up their stellar mass in much the same way as their intermediate-mass counterparts; this level is consistent with the ensemble of generally rising, scale-free SFHs discussed by [Kelson \(2014\)](#) and consistent with nonlinear gravitational collapse ([Kelson et al. 2020](#)).
- We compared nebular A_V (from the Balmer decrement) and stellar continuum A_V (from SED fitting) for both samples. IMGs show a clear increase in A_V with stellar mass for both nebular and stellar components, while LMGs exhibit lower

overall attenuation and a weaker dependence on M_* . This difference is consistent with the lower dust content expected in low-metallicity, low-mass galaxies (e.g., [Salim & Narayanan 2020](#)). In all cases, stellar A_V is lower than nebular A_V , in line with the two-component dust model.

- The ratio $E(B-V)_{\text{nebular}}/E(B-V)_{\text{stellar}}$ for both LMGs and IMGs is close to the canonical factor of 2.27 from [Calzetti et al. \(2000\)](#). We find no significant correlation of this ratio with stellar mass in either sample, consistent with previous results for more massive galaxies (e.g., [Reddy et al. 2015](#); [Shivaei et al. 2020b](#)). When examined as a function of sSFR, the ratio shows a mild tendency to increase toward higher sSFR for IMGs. This trend is qualitatively consistent with scenarios in which dust is preferentially concentrated in the youngest star-forming regions, leading to greater obscuration of nebular emission relative to the stellar continuum (e.g., [Reddy et al. 2015](#)). For LMGs, by contrast, the median ratio remains approximately constant, suggesting that the stellar feedback disperses birth clouds efficiently in shallow potentials so that the nebular-to-stellar reddening ratio is roughly sSFR-invariant.

Future work will build on this analysis by incorporating gas-phase metallicity measurements and high-resolution morphological information to place the observed dust attenuation trends in a broader physical context, enabling a more direct connection between galaxy morphology, chemical enrichment, and star formation properties in low-mass systems.

ACKNOWLEDGEMENT

We thank the anonymous referee for providing insightful comments and suggestions that improved the quality of this work. This paper includes data gathered with the 6.5-meter Magellan Telescopes at Las Campanas Observatory, Chile. We thank the staff for their dedication and support.

REFERENCES

- Arnouts, S., Moscardini, L., Vanzella, E., et al. 2002, *MNRAS*, 329, 355
- Baldry, I. K., Driver, S. P., Loveday, J., et al. 2012, *MNRAS*, 421, 621
- Bisigello, L., Caputi, K. I., Grogin, N., & Koekemoer, A. 2018, *A&A*, 609, A82
- Boogaard, L. A., Brinchmann, J., Bouché, N., et al. 2018, *A&A*, 619, A27
- Brammer, G. B., van Dokkum, P. G., & Coppi, P. 2008, *ApJ*, 686, 1503
- Bruzual, G., & Charlot, S. 2003, *MNRAS*, 344, 1000

- Byler, N., Dalcanton, J. J., Conroy, C., & Johnson, B. D. 2017, *ApJ*, 840, 44
- Calzetti, D., Armus, L., Bohlin, R. C., et al. 2000, *ApJ*, 533, 682
- Carnall, A. C., McLure, R. J., Dunlop, J. S., & Davé, R. 2018, *MNRAS*, 480, 4379
- Charlot, S., & Fall, S. M. 2000, *ApJ*, 539, 718
- Chartab, N., Newman, A. B., Rudie, G. C., Blanc, G. A., & Kelson, D. D. 2024, *ApJ*, 960, 73
- Chevance, M., Kruijssen, J. M. D., Hygate, A. P. S., et al. 2020, *MNRAS*, 493, 2872
- Cullen, F., McLure, R. J., Khochfar, S., et al. 2018, *MNRAS*, 476, 3218
- De Vis, P., Jones, A., Viaene, S., et al. 2019, *A&A*, 623, A5
- Dekel, A., & Silk, J. 1986, *ApJ*, 303, 39
- Dressler, A., Bigelow, B., Hare, T., et al. 2011, *PASP*, 123, 288
- Edgeworth, F. Y. 1888, *The London, Edinburgh, and Dublin Philosophical Magazine and Journal of Science*, 25, 184
- Emami, N., Siana, B., Weisz, D. R., et al. 2019, *ApJ*, 881, 71
- Ferland, G. J., Chatzikos, M., Guzmán, F., et al. 2017, *RMxAA*, 53, 385
- Gallagher, III, J. S., Hunter, D. A., & Tutukov, A. V. 1984, *ApJ*, 284, 544
- Garn, T., & Best, P. N. 2010, *MNRAS*, 409, 421
- Geha, M., Blanton, M. R., Yan, R., & Tinker, J. L. 2012, *ApJ*, 757, 85
- Geha, M., Mao, Y.-Y., Wechsler, R. H., et al. 2024, *ApJ*, 976, 118
- Gordon, K. D., Clayton, G. C., Misselt, K. A., Landolt, A. U., & Wolff, M. J. 2003, *ApJ*, 594, 279
- Hemmati, S., Mobasher, B., Darvish, B., et al. 2015, *ApJ*, 814, 46
- Horne, K. 1986, *PASP*, 98, 609
- Ilbert, O., Arnouts, S., McCracken, H. J., et al. 2006, *A&A*, 457, 841
- Kashino, D., Silverman, J. D., Rodighiero, G., et al. 2013, *ApJL*, 777, L8
- Kelson, D. D. 2003, *PASP*, 115, 688
- . 2014, *arXiv e-prints*, arXiv:1406.5191
- Kelson, D. D., Illingworth, G. D., van Dokkum, P. G., & Franx, M. 2000, *ApJ*, 531, 159
- Kelson, D. D., Abramson, L. E., Benson, A. J., et al. 2020, *MNRAS*, 494, 2628
- Kennicutt, Robert C., J. 1998, *ARA&A*, 36, 189
- Koller, M., Ziegler, B., Ciocan, B. I., et al. 2024, *A&A*, 689, A315
- Kriek, M., van Dokkum, P. G., Labbé, I., et al. 2009, *ApJ*, 700, 221
- Kroupa, P. 2001, *MNRAS*, 322, 231
- Kurczynski, P., Gawiser, E., Acquaviva, V., et al. 2016, *ApJL*, 820, L1
- Lee, J. C., Gil de Paz, A., Tremonti, C., et al. 2009, *ApJ*, 706, 599
- Leja, J., Tacchella, S., & Conroy, C. 2019, *ApJL*, 880, L9
- Leja, J., Speagle, J. S., Ting, Y.-S., et al. 2022, *ApJ*, 936, 165
- Lin, X., Cai, Z., Zou, S., et al. 2023, *ApJL*, 944, L59
- Mehta, V., Teplitz, H. I., Scarlata, C., et al. 2023, *ApJ*, 952, 133
- Mitra, S., Davé, R., & Finlator, K. 2015, *MNRAS*, 452, 1184
- Muzzin, A., Marchesini, D., Stefanon, M., et al. 2013a, *ApJS*, 206, 8
- . 2013b, *ApJ*, 777, 18
- Noeske, K. G., Weiner, B. J., Faber, S. M., et al. 2007, *ApJL*, 660, L43
- Oke, J. B., & Gunn, J. E. 1983, *ApJ*, 266, 713
- Osterbrock, D. E., & Ferland, G. J. 2006, *Astrophysics of gaseous nebulae and active galactic nuclei*
- Pacifici, C., Kassin, S. A., Weiner, B. J., et al. 2016, *ApJ*, 832, 79
- Pacifici, C., Iyer, K. G., Mobasher, B., et al. 2023, *ApJ*, 944, 141
- Patel, S. G., Kelson, D. D., Abramson, L. E., Sattari, Z., & Lorenz, B. 2023, *ApJ*, 945, 93
- Peeples, M. S., & Shankar, F. 2011, *MNRAS*, 417, 2962
- Price, S. H., Kriek, M., Brammer, G. B., et al. 2014, *ApJ*, 788, 86
- Qin, J., Zheng, X. Z., Wuyts, S., Pan, Z., & Ren, J. 2019, *ApJ*, 886, 28
- Reddy, N. A., Kriek, M., Shapley, A. E., et al. 2015, *ApJ*, 806, 259
- Reddy, N. A., Oesch, P. A., Bouwens, R. J., et al. 2018, *ApJ*, 853, 56
- Rémy-Ruyer, A., Madden, S. C., Galliano, F., et al. 2014, *A&A*, 563, A31
- Renzini, A., & Peng, Y.-j. 2015, *ApJL*, 801, L29
- Robertson, B. E., Ellis, R. S., Dunlop, J. S., McLure, R. J., & Stark, D. P. 2010, *Nature*, 468, 49
- Salim, S., Boquien, M., & Lee, J. C. 2018, *ApJ*, 859, 11
- Salim, S., & Narayanan, D. 2020, *ARA&A*, 58, 529
- Salmon, B., Papovich, C., Long, J., et al. 2016, *ApJ*, 827, 20
- Scoville, N., Aussel, H., Brusa, M., et al. 2007, *ApJS*, 172, 1
- Shivaei, I., Darvish, B., Sattari, Z., et al. 2020a, *ApJL*, 903, L28
- Shivaei, I., Reddy, N., Rieke, G., et al. 2020b, *ApJ*, 899, 117

- Sparre, M., Hayward, C. C., Feldmann, R., et al. 2017, MNRAS, 466, 88
- Speagle, J. S., Steinhardt, C. L., Capak, P. L., & Silverman, J. D. 2014, ApJS, 214, 15
- Tolstoy, E., Hill, V., & Tosi, M. 2009, ARA&A, 47, 371
- Tremonti, C. A., Heckman, T. M., Kauffmann, G., et al. 2004, ApJ, 613, 898
- Virtanen, P., Gommers, R., Oliphant, T. E., et al. 2020, Nature Methods, 17, 261
- Weaver, J. R., Kauffmann, O. B., Ilbert, O., et al. 2022, ApJS, 258, 11
- Weisz, D. R., Dolphin, A. E., Skillman, E. D., et al. 2014, ApJ, 789, 148
- Weisz, D. R., Johnson, B. D., Johnson, L. C., et al. 2012, ApJ, 744, 44
- Whitaker, K. E., Franx, M., Leja, J., et al. 2014, ApJ, 795, 104
- White, S. D. M., & Rees, M. J. 1978, MNRAS, 183, 341